Nanoscale Transformations in Metastable, Amorphous, Silicon-Rich Silica

Adnan Mehonic,* Mark Buckwell, Luca Montesi, Manveer Singh Munde, David Gao, Stephen Hudziak, Richard J. Chater, Sarah Fearn, David McPhail, Michel Bosman, Alexander L. Shluger, and Anthony J. Kenyon*

Functional oxides are fundamental to modern microelectronics as high quality insulators, transparent conductors, electroluminescent and electrochromic materials, amongst other applications. Considerable effort over several decades has yielded high quality stoichiometric defect-free materials now ubiquitous in complementary metal oxide semiconductor (CMOS) devices. However, substoichiometric amorphous oxides are increasingly important across a range of new technologies. Modern devices incorporate few-nanometer thick layers in which electrical stress can be extreme. Despite this, the oxide is generally assumed to remain largely structurally inert under normal operating conditions. However, we show here, through electrical and structural characterization, along with density functional theory (DFT) and Monte Carlo modeling (Supporting Information), that realistic device voltages can generate surprisingly major structural and chemical changes. In some cases these are reversible; in others they are permanent precursors to dielectric breakdown. Our results have major implications for the electronic and photonic applications of substoichiometric amorphous oxides – rather than passive, stable insulators they are instead highly dynamic electrically manipulated materials.

Despite their increasing prevalence, the dynamic response of amorphous substoichiometric oxides to electrical stresses encountered in applications including resistance switching,[1]

Dr. A. Mehonic, M. Buckwell, L. Montesi,
M. S. Munde, Dr. S. Hudziak, Prof. A. J. Kenyon
Department of Electronic and Electrical Engineering
UCL
Torrington Place, London WC1E 7JE, UK
E-mail: a.mehonic@ee.ucl.ac.uk;
t.kenyon@ee.ucl.ac.uk
M. S. Munde, Dr. M. Bosman
Institute of Materials Research and Engineering
2 Fusionopolis Way, Singapore, 138634
Dr. D. Gao, Prof. A. L. Shluger
Department of Physics and Astronomy and London
Centre for Nanotechnology
UCL
Gower Street, London WC1E 6BT, UK
Dr. R. J. Chater, Dr. S. Fearn, Prof. D. McPhail
Department of Materials
Imperial College London
South Kensington Campus, London SW7 2AZ, UK

electroluminescent devices,[2] electrochromic windows,[3] and transparent amorphous conductors[4] remains poorly understood. Abrupt changes of resistance in response to electrical stress are hallmarks of correlated electron and ion dynamics and an obvious manifestation of structural dynamics; such phenomena have been reported in a variety of oxides with a range of stoichiometries in different applications. Materials studied include indium tin oxide, zinc, vanadium, nickel, and titanium oxides, and silicon oxide, all of which have a variable degree of substoichiometry that affects the dynamics of resistance change. Here, we employ a suite of structural characterization techniques, including bias-induced resistance changes, to probe dynamic structural changes in amorphous oxides. Abrupt resistance changes are not necessarily central to device functionality, and in some cases, such as electroluminescence, are detrimental. Nevertheless, they demonstrate an extreme response to electrical stress. Silicon oxide, which we study here, is a technologically important oxide representative of the broader class of metastable amorphous oxides. It is historically one of the most studied materials, and the remarkable dynamics that we uncover are thus all the more surprising.

Existing models for defect generation and electrical breakdown in oxides are often restricted to crystalline and stoichiometric materials; amorphous oxides present a formidable modeling challenge. Nevertheless, recent work on resistance switching highlights local structural and chemical changes driven by sub-breakdown electrical stress. Research into resistance changes in silicon oxide dates back to the 1960s and 1970s, when irreversible electrical breakdown was widely studied.[5–8] More recently, there have been reports of intrinsic reversible (soft) breakdown of silicon oxide,[9–11] usually ascribed to the formation of chains of oxygen vacancies[12] produced by field-driven movement of oxygen ions. The reversibility of these changes is of the greatest interest, as it probes the dynamics of oxides under controlled stress and provides a model for the initial stages of irreversible dielectric breakdown. In terms of applications, nonvolatile resistive random access memory (RRAM)[1] or analogue neuromorphic devices[13,14] are important technological areas that exploit reversible dynamic changes in oxide local structure. However, they are by no means the only applications relying on electrically stressed amorphous oxides.[2–4] The observation of quantized conductance in electrically stressed silicon oxide suggests further applications in quantum technology[15] while, in other fields, studies of electroluminescence from silicon-rich silicon oxide demonstrate that its optical properties depend critically on the sequence of applied voltage stress; over-stressing produces permanent

COMMUNICATION

optical and electrical changes without destroying the devices, the origins of which are uncertain.[2] Dramatic resistance changes are thus a manifestation of complex oxide dynamics, which we further elucidate in this paper.

Here we demonstrate that field-driven movement of oxygen ions causes changes in oxide structure on a much larger scale than previously thought. We definitively demonstrate oxygen release from stressed films and we show that these changes are apparent at electric fields comparable to those routinely used in microelectronic and photonic devices. A comprehensive understanding of dynamic structural changes thus promises to enable new technologies in a range of fields as well as providing an understanding of the early stages of catastrophic oxide breakdown. Detailed electrical measurements are one of the most sensitive techniques available to probe the formation of defect states in oxides – for example in studies of trap generation in negative bias temperature instability in metal oxide semiconductor field-effect transistors (MOSFETs).[16] We therefore used these as a starting point for our study.

We begin by using transmission electron microscopy (TEM) to probe variations in silicon and oxygen distribution, and density variation in both pristine and electrically stressed samples. Our test samples are metal–insulator–metal structures with titanium nitride (TiN) electrodes sandwiching a 37 nm thick, amorphous, silicon-rich silica (SiO_x, $x \approx 1.3$) layer (**Figure 1**a, inset). Our electrical stress protocol is illustrated in Figure 1a (top left), which shows the electrical response of a typical sample to a voltage sweep with a current compliance limit set. An abrupt resistance change at around 6 V suggests structural changes within the oxide – perhaps related to the formation of a conductive filament. This is often referred to as electroforming, with a current limit applied in this case to prevent irreversible breakdown. Setting a current limit prevents us from measuring the speed of resistance changes, so in separate tests using pulsed biasing and no current limit we measured transitions to occur on the order of tens of nanoseconds (further details in the Supporting Information and a report by Montesi et al.[17]). Figure 1b shows a cross-sectional dark field scanning transmission electron microscopy (STEM)
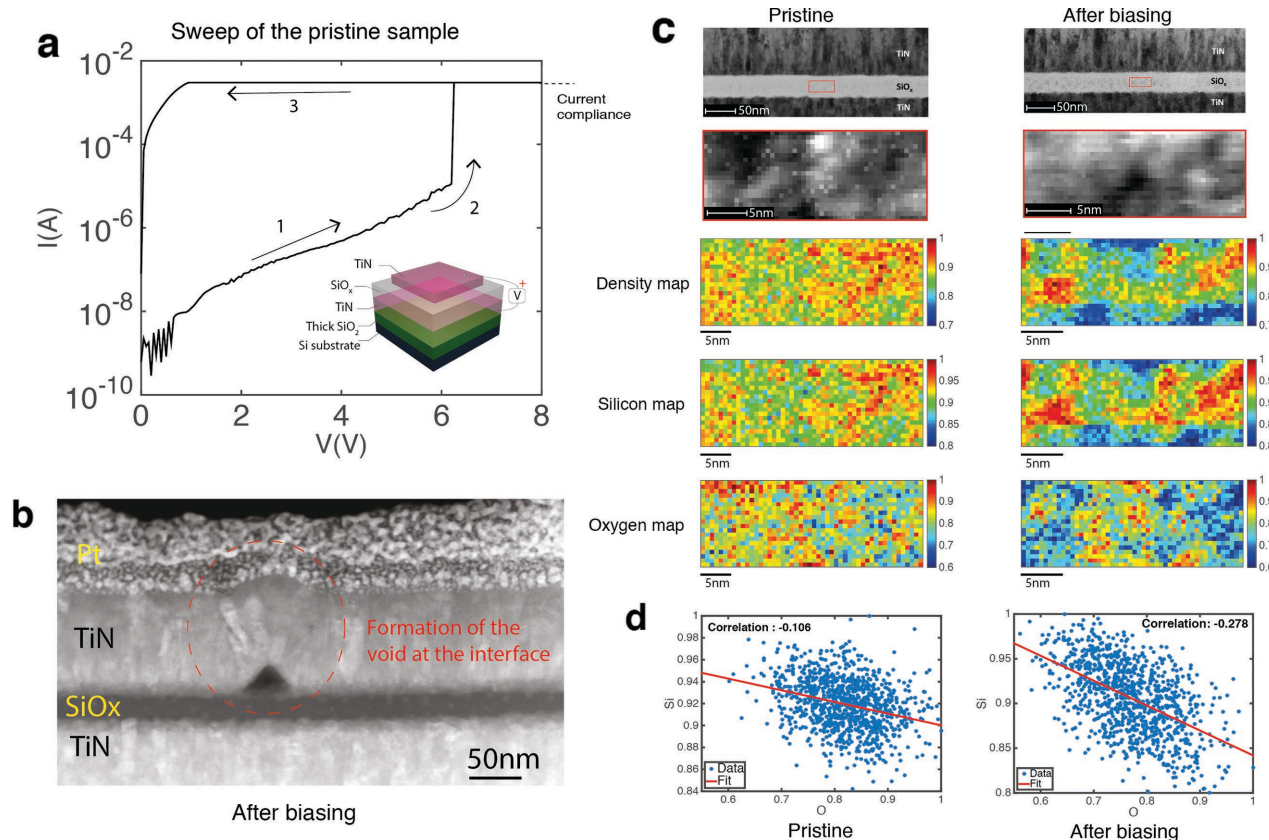

Figure 1. Electrical stress of a test structure, and resulting structural changes. a) Typical current/voltage curve showing an abrupt resistance change. Inset: schematic representation of a test structure. b) Dark-field TEM image of a stressed sample, highlighting a void formed at the interface between the SiO_x and the top TiN electrode, along with a corresponding distortion of the top electrode. c) left: Dark-field STEM cross-sectional image of an unstressed sample. There is some inhomogeneity in the SiO_x layer, likely because the layer is silicon rich. Right: corresponding image of a stressed sample, showing an increase in the SiO_x inhomogeneity. The sample was biased in an ambient environment; biasing conditions are those in the curve shown in (a). The red rectangles indicate the scale of the region analyzed in the images below. Top to bottom: relative density, silicon and oxygen maps of a section of the oxide layer in unstressed and stressed material (left and right columns, respectively). Inhomogeneity is now clear as variations in density and composition; the ratio of high to low density in the unstressed material is 1.26, which increases to 1.47 in the stressed material. We see ≈10 nm diameter clusters of high-density material that is more silicon-rich than the background. d) Scatter graphs of silicon signal against oxygen signal for the unstressed and stressed oxide (left and right, respectively). The increase in negative correlation following biasing indicates segregation into more silicon-rich regions.

image of a sample following the application of electrical stress as illustrated in Figure 1a in which a dark region appears at the upper SiO_x/TiN interface. The dark appearance of the structure implies low density (a void). We did not see similar structures in the unstressed film.

Figure 1c top left shows a dark-field STEM cross section of unstressed oxide. Nanometer-scale inhomogeneity is evident as contrast variations. This is unsurprising, as the oxide is substoichiometric. However, a similar image of a stressed region (Figure 1c, top right) suggests, remarkably, that the applied field has greatly enhanced this inhomogeneity. Below the STEM cross sections are normalized relative density maps of inhomogeneity, and separate chemical maps for silicon and oxygen at the nanometer scale (see the Experimental Section). Regions of higher density are larger within stressed material, and the increased contrast between high and low density regions suggests field-driven reordering of the random amorphous oxide.

The strong correlation between silicon signal and density in the unstressed material, along with the pattern of small (≈1 nm) regions of high density in Figure 1c, suggests that excess silicon in the pristine oxide is partly in the form of very small silicon inclusions. Following electrical stress, the matrix separates into strongly substoichiometric regions surrounded by more oxygen-rich suboxides. This is reminiscent of the aggregation of small silicon inclusions into larger suboxide clusters reported in annealing studies of SiO_x for photonic applications.[18]

Figure 2a shows Si2p X-ray photoelectron spectra (XPS) of a sample in the pristine state, and after positive bias. The pristine oxide bulk contains predominantly suboxide silicon configurations and elemental silicon. Electroforming increases the Si^0 contribution from ≈25% to ≈34% of the total signal, with small decreases in contributions from Si^{1+}, Si^{3+}, and Si^{4+}, signifying oxide reduction. The oxygen content decreases by 7% after
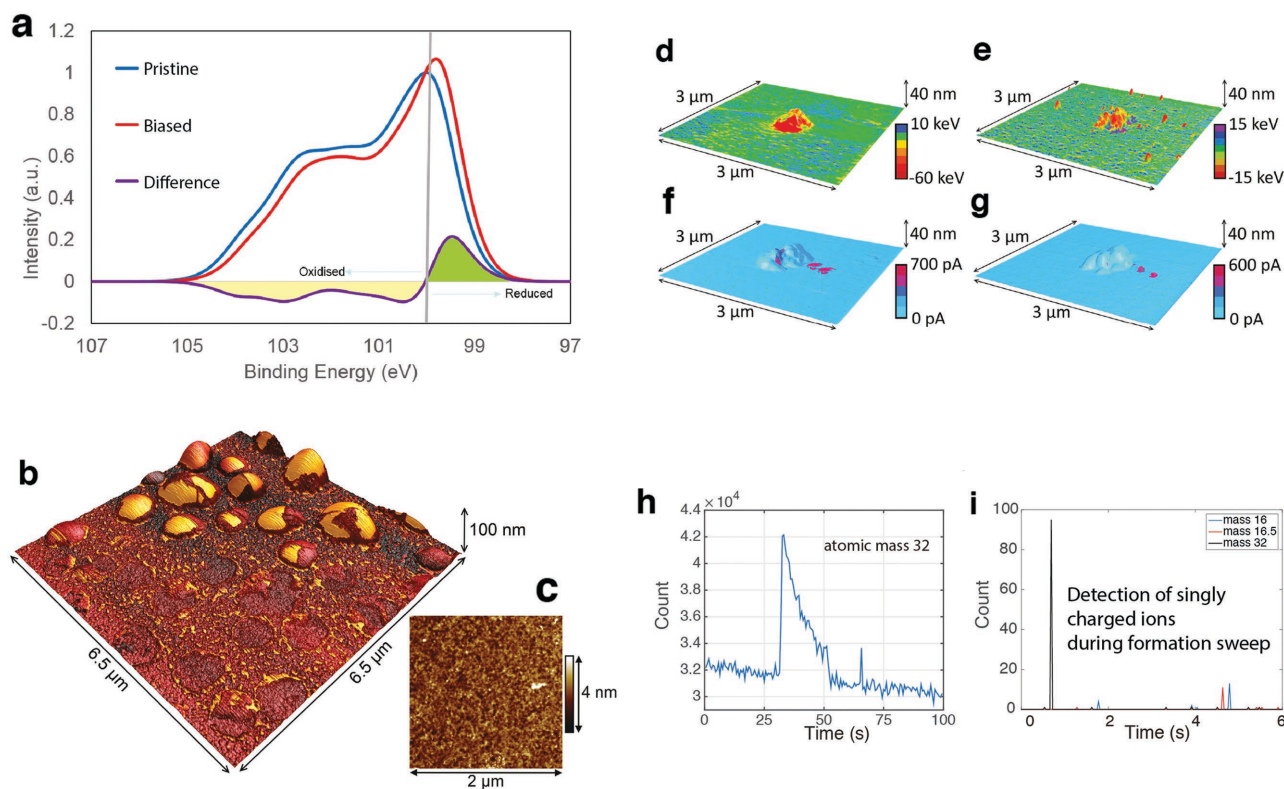

Figure 2. a) XPS Si2p spectra for pristine and electroformed SiO_x. The difference spectrum shows an overall chemical reduction of the oxide as a result of electroforming. This is confirmed by deconvolution of the pristine and formed spectra into contributions from individual Si oxidation states (the Supporting Information). b) Atomic force microscopy (AFM) topography image of the surface of SiO_x following electroforming. Bubbles are semi-permanent features, persisting after electroforming and many subsequent cycles between high and low resistance states, and are evidenced by the presence of both intact bubbles and residual menisci from those that have burst. The color scale represents cantilever phase, overlaid onto the topography to highlight small-scale surface features. c) Topography of pristine SiO_x. The surface is very flat with a root-mean-square (RMS) roughness of 0.2 nm. d) Energy dissipation mapped onto topography for a positive-bias initial stress (electroform). The central feature is permanent and softer than the surrounding, pristine material, shown by the greater energy dissipated on the feature compared to the surroundings. e) Corresponding map for a negative-bias electroform. The feature is again permanent and softer than the pristine material, but not to as large an extent. f,g) Conductive atomic force microscopy (cAFM) conductivity maps for positive- and negative-bias initial stresses, respectively. Conductive regions appear local to the feature. h) RGA time scan taken during voltage bias of pristine oxide showing increased counts at mass 32 (O_2) during voltage stress. Note that this sample did not exhibit an abrupt change in resistance, indicating correlation with electrical stress rather than with resistance changes. i) Time scans of mass fragments emitted during electrical bias of pristine material. Here the secondary-ion mass spectrometry SIMS detector was used in RGA mode; all detected fragments are ions. A peak at mass 32 indicates emission of superoxide ions; masses 16 and 16.5 show no significant increases, ruling out oxygen ions or background noise.

COMMUNICATION

electroforming. Both observations are consistent with field-driven dissociation of oxygen from Si–O bonds. When bias is applied, asymmetric oxygenated Si configurations, in particular Si^{1+} and Si^{3+}, are reduced throughout the layer, leaving Si-rich material containing elemental Si^0 inclusions (see the Supporting Information).

Buckwell et al.[19] and others[20,21] have observed surface distortions following electroforming and subsequent cycling between resistance states, which suggest major structural changes. Distortions have been reported in a number of oxides, including titanium oxide[19] and strontium titanate.[22] Indeed, reports of surface deformation and possible gaseous emission from electrically stressed oxides date back to the 1960s,[6] but their source remains a subject of speculation. If a top electrode is present, deformations appear on its surface; if the oxide is biased using a probe tip, they occur at the point of contact. Such deformations have been attributed to oxygen release, but have not been studied in detail. To elucidate the mechanism of surface distortion, we applied 60 ns voltage pulses of +20 or −20 V at separate locations, allowing us to study both positive and negative electrical biases, controlling pulse duration to avoid breakdown. We often observed bubble-like features with diameters up to hundreds of nanometers around the probe contact point (Figure 2b). These did not persist in a vacuum and were readily removed with solvent washing. Atomic force microscopy (AFM) measurements of these bubbles could only be made in tapping mode; contact-based modes burst them, leaving residual menisci.

In some cases, following electrical stress we observed more permanent bumps up to a few hundred nanometers wide and ≈40 nm high at the bias point. On structures with top contacts that we cycled through resistance states repeatedly, such bumps persisted through many cycles. Energy dissipation scans (Figure 2d,e) indicate that the conductive region is softer than the pristine oxide. Raised regions dissipate more energy than the pristine surface for both positive and negative stress. Some regions dissipate less energy, suggesting localized hardening. Conductive AFM shows correlation between surface distortion and regions of increased conductivity (Figure 2f,g). We can surmise that both bias polarities drive an expansion of the oxide that correlates with increases in local conductivity, but under positive bias the material also becomes much softer. This suggests current-driven Joule heating distorts the local structure, generating surface deformation and regions of different hardness.

In situ electrical forming experiments in a vacuum chamber with a secondary-ion mass spectrometer (SIMS) detector operating in residual gas analyzer (RGA) mode demonstrate correlation between electrical stress and oxygen emission. Figure 2h shows a plot of counts against time for detected ions of mass 32 (molecular oxygen), showing a transient as the voltage is ramped. The only other mass fragment detected was mass 28, corresponding to CO, likely formed through the oxidation of surface-based carbon contaminants. The lack of other nitrogen-containing fragments excludes the possibility that this is nitrogen. We observed that repeated resistance cycling was more difficult in vacuum than in air; samples often became stuck in a very low resistance state and could not be returned to the high resistance state. Such behavior, reported previously

by Wang et al.[23] is consistent with loss of oxygen from samples in vacuum.

Using the SIMS detector conventionally allows detection of charged species. We electroformed the sample in situ and counted ions at mass 16 (O^-), 16.5 (background), and 32 (superoxide ions, O_2^-). No increases at masses 16 and 16.5 were detected. However, a burst at mass 32 (Figure 2i) confirmed emission of superoxide ions, which may be readily generated at metal oxide, semiconducting oxide, and silicon oxide surfaces.[24,25] As we operate under electron injection, ions may escape from the oxide while maintaining overall charge neutrality. It is tempting to speculate that electrostatic repulsion between superoxide ions at least partly explains the large surface deformations observed in Figure 2a. We note that, as we have reported previously,[18] our samples show similar behavior in both biases: changes in conductivity correlate with oxygen release. It is to be expected that, whatever the overall direction of movement of oxygen ions – toward the top electrode for positive bias, and toward the bottom electrode for negative bias – a similar picture of segregation of oxygen will be seen.

Our experimental data pose several important questions: how is it that oxygen movement can occur on the tens of nanoseconds timescale characteristic of the observed resistance changes? What causes the large surface distortions that correlate with oxygen movement and release? Finally, how can we explain the emission of superoxide ions? Previous studies address these questions only partially. Excess oxygen has been predicted to exist as O_2 interstitials, peroxy linkages, threefold configurations, and double bridges[26,27] with interstitial O_2 molecules,[28] the most stable surplus oxygen species in crystalline and amorphous SiO_2. Calculations predict an average barrier of 0.7 eV for O_2 molecule diffusion in a-SiO_2.[27,29] However, oxygen atoms are most stable in the form of peroxy linkages,[30] which diffuse through crystalline SiO_2 with a barrier of 1.3 eV.[31] We have previously demonstrated that pristine SiO_x is indeed rich in peroxy linkages.[32] However, these diffusion barriers are too high to account for the rapid oxygen movement we observe. It is most likely stimulated by electron injection. At biases typical of our experiments, electrons tunnel into the conduction band of a-SiO_2 (**Figure 3**a). They can then access defect states within the oxide, producing negatively charged defects. Theoretical studies indeed predict that negatively charged oxygen diffuses rapidly in crystalline SiO_2, with a much smaller barrier of 0.3 eV.[26]

We further examined the stability of oxygen defects in amorphous oxide using density functional theory (DFT). The formation energies of neutral and negatively charged interstitial oxygen atoms and molecules were calculated using neutral and negatively charged periodic unit cells of a-SiO_2. We compared the formation energies of these defects as a function of Fermi level (see the Supporting Information). Our results demonstrate that, under electron injection, interstitial O_2 molecules can trap up to two electrons, greatly weakening the bond between oxygen atoms and resulting in oxygen ion defects in the double bridge configuration becoming more energetically favorable than negatively charged interstitial molecules. Importantly, we predict that oxygen in the double bridge configuration can diffuse through a-SiO_2 with diffusion barriers on the order of 0.2 eV. At room temperature
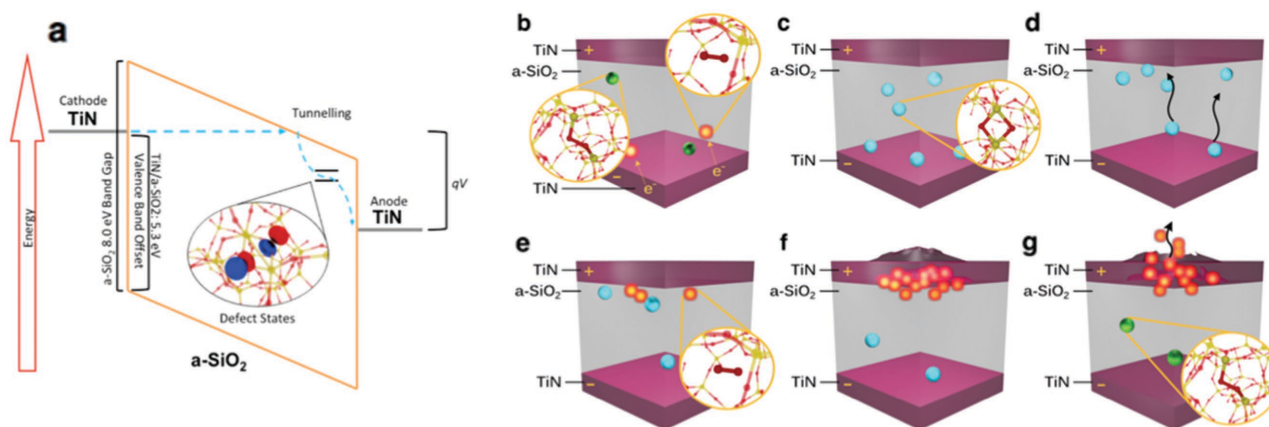
Figure 3. A model for the rapid movement of oxygen and the subsequent release of oxygen molecules. a) Schematic representation of electron injection conditions. b) Existing oxygen defects, including peroxy linkages and interstitial molecules, are distributed throughout the oxide layer. c) Existing defects rearrange into the double bridge configuration under electron injection conditions. d) A lower diffusion barrier results in the rapid migration of oxygen ions to the positive electrode. e) Ions discharge and recombine into oxygen molecules at the TiN/a-SiO$_2$ interface. f) A build-up of oxygen begins to deform the TiN layer. g) Eventually the bubble ruptures to release detectable oxygen molecules.

these negatively charged ions move quickly toward the positive electrode.

Using these data, we propose a qualitative mechanism for rapid oxygen movement through a-SiO$_2$ under electron injection, subsequent deformation of the TiN surface, and release of O$_2$ molecules, as shown in Figure 3. Initially, the oxide contains some concentration of oxygen defects in the form of interstitial molecules and peroxy linkages, as illustrated in Figure 3b. These are distributed evenly throughout the amorphous material and diffuse slowly at room temperature due to large diffusion barriers. Under applied bias, these defects rearrange into the double bridge configuration (Figure 3c). Bias application may generate additional defects; however, the mechanisms responsible are not known and will be the subject of a future study. In this configuration, the diffusion barrier is greatly reduced and oxygen ions begin to move much faster toward the positive electrode (Figure 3d). Prior theoretical studies of the interaction between oxygen and the TiN surface demonstrate that the barrier for an oxygen atom to diffuse into TiN is significant.[33–35] Arriving oxygen anions are thus likely to be trapped at the TiN/a-SiO$_2$ interface. They discharge at the anode and form O$_2$ molecules (Figure 3e). As more O$_2$ molecules are formed, bubbles form at the interface, which distort the TiN surface (Figure 3f). With enough build-up, they burst to release detectable O$_2$ molecules (Figure 3g). Since some molecules remain in contact with the a-SiO$_2$ surface within the bubble, they may be released as superoxide ions, via previously reported mechanisms.[24,25]

In addition to the emission of O$_2$ molecules, the migration of oxygen ions within the oxide is also responsible for the significant changes in electrical properties. We therefore set up a self-consistent stochastic model to link the movement of oxygen ions to probe large-scale changes in oxide structure generated by electrical stress (see the Supporting Information). This is in contrast to other Monte Carlo models in the literature that concentrate solely on conductive filament formation.

In summary, we have demonstrated unambiguously how electrical stress drives movement of oxygen in amorphous substoichiometric silicon oxide, and how this movement produces unexpectedly major structural rearrangement and local reordering. **Figure 4** summarizes the behaviour we have identified. Our study provides five novel conclusions: field-driven oxygen migration is surprisingly global; this movement can result in oxygen emission; some of the emitted oxygen is in the form of superoxide ions; bubbles form at the interface between the oxide and electrode, and we propose a new model for the generation of mobile oxygen in amorphous material. Our results shed light on the microscopic source of oxide electrical resistance changes, as well as the early stages of destructive electrical breakdown. They may also help explain previously reported changes in the optical properties of SiO$_x$ following voltage stress.[2] Most significantly, they reveal the highly dynamic nature of amorphous silicon oxide and, by extension, other substoichiometric amorphous oxides, under electrical bias. The electric fields we have used are well below those required for destructive breakdown, and are similar to those routinely encountered in applications such as electroluminescence, electrochromic windows, and the electroforming step of resistive RAM. Nevertheless, in some cases we have deliberately biased the test structures hard in order to illustrate the extent of oxygen movement that can be achieved. This does not imply that devices incorporating amorphous oxides are inherently unstable or prone to early failure under normal use so long as proper account is taken of the effect of the application of high fields over long durations. Evidence that such effects can be mitigated comes from results showing extreme endurance and cycling of amorphous SiO$_x$ resistive RAM.[36] A further important point is that our results demonstrate that abrupt resistance changes arising from conductive filament formation are the end point of large-scale changes in oxygen distribution; it is these early changes that are most significant for the majority of applications of amorphous oxides. Movement of oxygen underpins a number of processes that are not necessarily correlated. These include segregation of oxygen-deficient regions, abrupt changes in resistance, and emission of oxygen and superoxide ions. Our results from this fundamental study are directly relevant to materials that are increasingly used in a range of
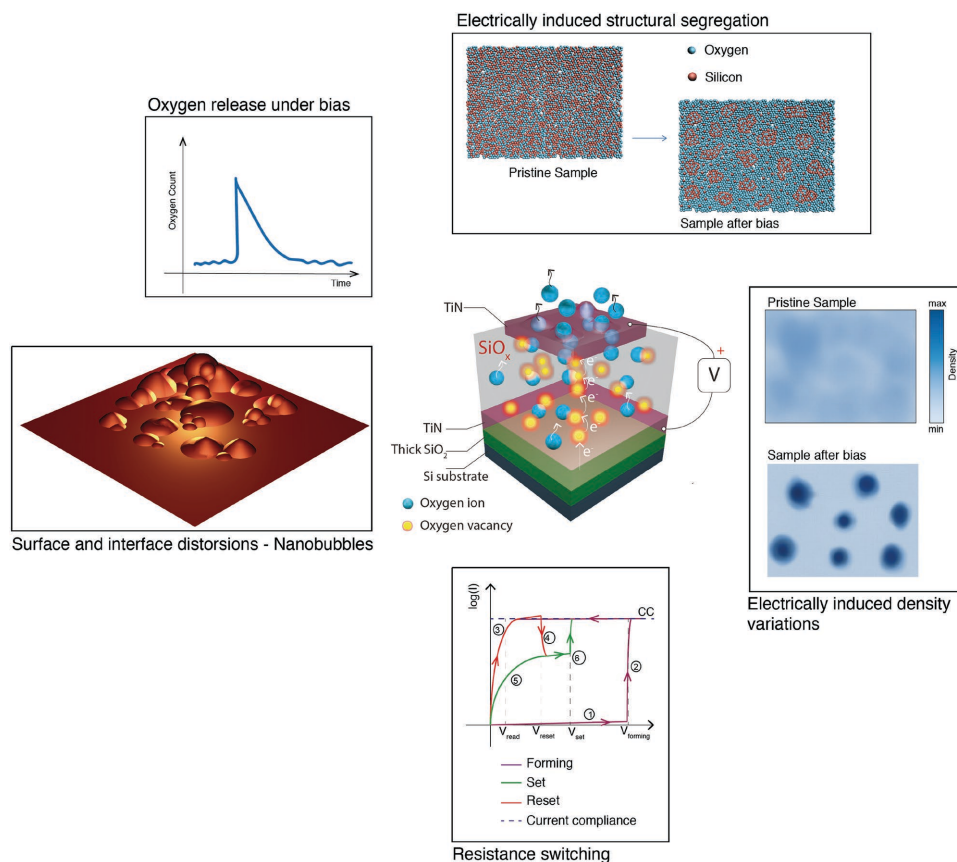
Figure 4. A schematic showing the multiple effects of electrical stress on amorphous oxides: movement of oxygen ions under electrical bias drives both compositional inhomogeneity and density variation. Eventually, large-scale movement can generate surface and interface distortions as oxygen builds up at interfaces, and ultimately oxygen may be emitted from the surface of the oxide. In some cases, these combined effects can drive abrupt changes in oxide resistance (resistance switching).

technologies, and demonstrate a surprising level of field-driven local reordering of a random oxide network.

Experimental Section

Test Structure Fabrication: Both electrodes and the oxide layer were deposited by magnetron co-sputtering onto a 3 inch silicon wafer with a 4 µm thermal oxide; TiN and SiO_x layers were 100 and 37 nm thick, respectively. Square top electrodes were defined by standard photolithographic techniques; sizes ranged from 400 to 10 µm². The excess Si content of the oxide, measured by X-ray photoelectron spectroscopy (XPS), was 11%, corresponding to a stoichiometry of approximately $SiO_{1.3}$. Full details of fabrication are given in the Supporting information.

Structural Studies: XPS data were gathered using a Thermo Scientific K-Alpha system at 10^{-8} Torr with a monochromated Al source at 1486.68 eV and a pass energy of 20 eV. Data were processed using CasaXPS v2.3.16 and spectra calibrated to the carbon C1s peak. To avoid having to remove the top electrode from a sample after electrical stress, the oxide was biased directly using a tungsten probe with a footprint of around 5 µm diameter as a top electrode, obtaining XPS spectra from the oxide below the probe. The sampled area was an ellipse with a long axis of 300 µm and a short axis of 150 µm. To ensure that any structural changes were large enough to be detected by the XPS system, voltage sweeps were applied at points located at 30 µm intervals in a

grid across a 300 µm square region. In contrast to the bulk of the oxide, the exposed oxide surface was nearly stoichiometric thanks to oxidation in ambient conditions.[32] This was not the case for structures with a top contact. Consequently, when biasing the oxide surface a higher voltage was applied in order to overcome the stoichiometric oxide tunneling barrier.

AFM and conductive AFM (cAFM) images were obtained using a Bruker Icon microscope in ambient conditions. AFM data were taken using silicon cantilevers and cAFM images were taken using platinum/iridium coated silicon cantilevers. The data were processed using NanoScope v9.1. To characterize the small surface features shown in Figure 2, conductive AFM scans were performed with the tip biased at −5 V relative to the microscope stage, which allowed us to measure conductivity without further changing the oxide by anodic oxidation. A series resistance of 178 kΩ was also added between the bottom electrode and the sample stage to complete the measurement circuit, reduce tip heating, and minimize current spikes from transient charging and discharging of surface defects during scans. In order to obtain the energy dissipation data, the mean spectrum of five force–distance curves was taken at every pixel. From this, the deviation between the approach and retract traces was integrated to yield the energy dissipated by the cantilever in the interaction between the tip and surface.

The reported AFM scans were performed in two modes, in each of which the measurements were repeated at different imaging angles. Measurements that involved different interactions could therefore be compared, and their consistency over time could be checked. The first mode, conductive AFM, may modify surfaces through anodic

oxidation. It was ensured that appropriate sample biases were used to enable measurements without modifying the surface. Additionally, such features in noncontact (tapping) mode[26] had been previously studied; their structure conformed to that reported here. Conductive AFM might also introduce imaging artifacts due to Coulomb repulsion. A second method was therefore used, PeakForce QNM, to study surface deformation and additional mechanical properties. Notably, the two scan modes reported here show similar features to each other and also to previous features scanned in noncontact mode. It is also noteworthy that these features are extremely robust and persist for many days following ultrasonication and vacuum environments. It could therefore be confidently said that the AFM measurements had no detectable effect on the sample surface.

For RGA and ion emission measurements, a single beam gallium ion gun system with an attached Hiden SIMS detector was employed. For detection of emitted gas the SIMS detector was used in an RGA mode, i.e. with a shielded low-energy electron beam source at the front end of the SIMS detector with its column polarized and optimized to detect positive ions only. In this mode no extraction voltage was applied to attract ions from close to the region of the entrance aperture of the SIMS detector.

The samples were biased using remotely actuated tungsten whiskers tapering to a diameter of 1 µm; the voltage was ramped and sample resistance measured at a low reading voltage (0.8 V, chosen to ensure no structural changes to the oxide during reading) after each increase in bias. Simultaneously, the mass spectrum of the chamber atmosphere was sampled over time.

Transmission Electron Microscopy: All specimens were prepared using an FEI Helios Nanolab 600 focused ion beam with initial deposition of a Pt layer. All STEM images were acquired at 80 kV (since at higher voltages damage occurs) on an FEI Titan in STEM mode.

All electron energy loss (EELS) spectra were acquired using a Gatan imaging filter (GIF): acquisition time for the stressed sample core loss spectrum was 200 ms; for the unstressed core loss spectrum 400 ms; for stressed and unstressed low loss spectra 200 ms. A 2.5 mm aperture was used in GIF with collection semi-angle of 25 mrad and beam convergence semi-angle of 14 mrad. Relative density maps were derived from EELS maps using a relative thickness map acquired by taking low loss spectra in addition to core loss spectra.[37] The assumption was made that the compatibility of this method with amorphous SiO_2 extends to SiO_x. The larger data scatter in the correlation plots for oxygen and density was due to a weaker O signal, since the Si and O signals were collected simultaneously.

The S/N ratios for EELS measurements were:

For stressed : $Si = 48.75, O = 4.77$

For unstressed : $Si = 102.95, O = 5.13$

Therefore it was safely above the detection limit.

DFT Calculations: Periodic models of a-SiO_2 containing a total of 216 atoms in each cell were previously produced using the ReaxFF force-field[38,39] implemented in the Large-scale Atomic/Molecular Massively Parallel Simulator (LAMMPS) code.[40] These structures were previously generated using classical molecular dynamics and a melt and quench procedure which is described in detail by El-Sayed et al.[41] The densities, distributions of Si–O bonds, distributions of Si–O–Si angles, and neutron structure factors of these models were evaluated[40] and showed excellent agreement with prior theoretical[42] and experimental[43] studies. DFT calculations performed using the Gaussians and Plane Waves[44] method as implemented in the CP2K code[45] were then used to further optimize these starting amorphous geometries, calculate their electronic structures, and study the properties of charged O defects in the material. The auxiliary density matrix method[46] was used in conjunction with the PBE0_RC_LRC[47] nonlocal functional. Finally, the MOLOPT basis set[48] was used along with the corresponding pseudopotentials (Goedecker–Teter–Hutter (GTH))[49] and a 400 Ry plane wave cutoff. This method produced an 8 eV band gap for a-SiO_2. Charge corrections were performed using the Lany Zunger method,[50] a dielectric constant of 3.9, and a Madelung constant of 2.8373 for the cubic cell.

Supporting Information

Supporting Information is available from the Wiley Online Library or from the author.

Acknowledgements

[1] R. Waser, M. Aono, *Nat. Mater.* **2007**, 6, 833.

[2] O. Jambois, Y. Berencen, K. Hijazi, M. Wojdak, A. J. Kenyon, F. Gourbilleau, R. Rizk, B. Garrido, *J. Appl Phys.* **2009**, 106, 063526.

[3] G. A. Niklasson, C. G. Granqvist. *J. Mater. Chem.* **2007**, 17, 127.

[4] T. Kamiya, H. Hosono, *NPG Asia Mater.* **2010**, 2, 15.

[5] D. R. Lamb, P. C. Rundle, *Brit. J. Appl. Phys.* **1967**, 18, 29.

[6] G. Dearnaley, A. M. Stoneham, D. V. Morgan, *Rep. Prog. Phys.* **1970**, 33, 1129.

[7] C. M. Osburn, D. W. Ormond, *J. Electrochem. Soc.* **1972**, 119, 591.

[8] M. Shatzkes, M. Av-Ron, R. M. Anderson, *J. Appl. Phys.* **1974**, 45, 2065.

[9] A. Mehonic, S. Cueff, M. Wojdak, S. Hudziak, O. Jambois, C. Labbe, B. Garrido, R. Rizk, A. J. Kenyon, *J. Appl. Phys.* **2012**, 111, 074507.

[10] A. Mehonic, M. Wojdak, S. Hudziak, R. Rizk, A. J. Kenyon, *Nanotechnology* **2012**, 23, 455201.

[11] Y. F. Chang, B. Fowler, Y. C. Chen, Y. T. Chen, Y. Wang, F. Xue, F. Zhou, J. C. Lee, *J. Appl. Phys.* **2014**, 116, 043708.

[12] A. Sawa, *Mater. Today* **2008**, 11, 28.

[13] G. Indiveri, B. Linares-Barranco, R. Legenstein, G. Deligeorgis, T. Prodromakis, *Nanotechnology* **2013**, 24, 384010.

[14] A. Mehonic, A. J. Kenyon, *Front. Neurosci.* **2016**, 10, 57.

[15] A. Mehonic, A. Vrajitoarea, S. Cueff, S. Hudziak, H. Howe, C. Labbe, R. Rizk, M. Pepper, A. J. Kenyon, *Sci. Rep.* **2013**, 3, 2708.

[16] D. K. Schroder, J. A. Babcock, *J. Appl. Phys.* **2003**, 94, 1.

[17] L. Montesi, M. Buckwell, K. Zarudnyi, L. Garnett, S. Hudziak, A. Mehonic, A. J. Kenyon, *IEEE Trans. Nanotechnol.* **2016**, 15, 428.

[18] I. F. Crowe, M. P. Halsall, O. Hulko, A. P. Knights, R. M. Gwilliam, M. Wojdak, A. J. Kenyon, *J. Appl. Phys.* **2011**, 109, 083534.

[19] M. Buckwell, L. Montesi, A. Mehonic, O. Reza, L. Garnett, M. Munde, S. Hudziak, A. J. Kenyon, *Phys. Status Solidi C* **2014**, 12, 211.

[20] D. S. Jeong, H. Schroeder, U. Breuer, R. Waser, *J. Appl. Phys.* **2008**, 104, 123716.

[21] J. J. Yang, F. Miao, M. D. Pickett, D. A. Ohlberg, D. R. Stewart, C. N. Lau, R. S. Williams, *Nanotechnology* **2009**, 20, 215201.

[22] K. Szot, W. Speier, G. Bihlmayer, R. Waser, *Nat. Mater.* **2006**, 5, 312.

[23] Y. Wang, X. Qian, K. Chen, Z. Fang, W. Li, J. Xu, *Appl. Phys. Lett.* **2013**, 102, 042103.

[24] M. Anpo, M. Che, B. Fubini, E. Garrone, E. Giamelli, M. Paganini, *Top. Catal.* **1999**, 8, 189.

[25] M. A. A. Schoonen, C. A. Cohn, E. Roemer, R. Laffers, S. R. Simson, T. O'Riordan, *Rev. Mineral. Geochem.* **2006**, 64, 179.

[26] G. Pacchioni, G. Ierano, *Phys. Rev. B* **1997**, 56, 7304.

[27] Y. G. Jin, K. J. Chang, *Phys. Rev. Lett.* **2001**, 86, 1793.

COMMUNICATION

[28] C. J. Sofield, A. M. Stoneham, *Semicond. Sci. Technol.* **1995**, *10*, 215.

[29] A. Bongiorno, A. Pasquarello, *Phys. Rev. B* **2004**, *70*, 195312.

[30] A. Shluger, E. Stefanovich, *Phys. Rev. B* **1990**, *42*, 9664.

[31] D. R. Hamann, *Phys. Rev. Lett.* **1998**, *81*, 3447.

[32] A. Mehonic, M. Buckwell, L. Montesi, L. Garnett, S. Hudziak, S. Fearn, R. Chater, D. McPhail, A. J. Kenyon, *J. Appl. Phys.* **2015**, *117*, 124505.

[33] J. Zimmermann, M. Finnis, L. Ciacchi, *J. Chem. Phys.* **2009**, *130*, 134714.

[34] J. Graciani, J. Sanz, T. Asaki, K. Nakamura, J. Rodriguez, *J. Chem. Phys.* **2007**, *126*, 244713.

[35] S. R. Bradley, K. P. McKenna, A. Shluger, *Microelectron. Eng.* **2013**, *109*, 346.

[36] H. Jiang, X. Y. Li, R. Chen, X. L. Shao, J. H. Yoon, X. Chu, C. S. Hwang, J. Zhao, *Sci. Rep.* **2016**, *6*, 22216.

[37] J. Thomas, J. Ramm, T. Gemming, *Micron* **2013**, *50*, 57.

[38] A. C. T. van Duin, A. Strachan, S. Stewman, Q. Zhang, X. Xu, W. Goddard, *J. Phys. Chem. A* **2003**, *107*, 3803.

[39] J. C. Fogarty, H. M. Aktulga, A. Y. Grama, A. C. T. van Duin, S. A. Pandit, *J. Chem. Phys.* **2010**, *132*, 174704.

[40] S. Plimpton, *J. Comput. Phys.* **1995**, *117*, 1.

[41] A. M. El-Sayed, M. B. Watkins, V. V. Afanas'ev, A. L. Shluger, *Phys. Rev. B* **2014**, *89*, 125201.

[42] K. Vollmayr, W. Kob, K. Binder, *Phys. Rev. B* **1996**, *54*, 15808.

[43] S. Susman, K. J. Volin, D. L. Price, M. Grimsditch, J. P. Rino, R. K. Kalia, P. Vashishta, G. Gwanmesia, Y. Wang, R. C. Liebermann, *Phys. Rev. B* **1991**, *43*, 1194.

[44] G. Lippert, J. Hutter, M. Parrinello, *Mol. Phys.* **1997**, *92*, 477.

[45] J. VandeVondele, M. Krack, F. Mohamed, M. Parrinello, T. Chassaing, J. Hutter, *Phys. Commun.* **2005**, *167*, 103.

[46] M. Guidon, J. Hutter, J. VandeVondele, *J. Chem. Theory Comput.* **2010**, *6*, 2348.

[47] M. Guidon, J. Hutter, J. VandeVondele, *J. Chem. Theory Comput.* **2009**, *5*, 3010.

[48] J. VandeVondele, J. Hutter, *J. Chem. Phys.* **2007**, *127*, 114105.

[49] S. Goedecker, M. Teter, J. Hutter, *Phys. Rev. B* **1996**, *54*, 1703.

[50] S. Lany, A. Zunger, *Phys. Rev. B* **2008**, *78*, 235104.